$11^{th}$ International Conference on Fracture Mechanics of Concrete and Concrete Structures
FraMCoS-11
J. M. Chandra Kishen, A. Ramaswamy, S. Ray and R. Vidyasagar (Eds)

https://doi.org/10.21012/FC11.092310

# X-RAY CT-BASED MEASUREMENTS OF RATE EFFECTS IN FRACTURE OF HIGH-PERFORMANCE CONCRETE

**AIDAN R CARLSON AND ERIC N LANDIS**

University of Maine
Orono, ME USA
e-mail: landis@maine.edu

**Key words:** X-ray CT, Fiber Reinforced Concrete, Rate Effects

**Abstract.** An experimental study was performed on different types of steel fiber reinforced concrete with the objective of measuring the changes in energy dissipation mechanisms as a function of loading rate and fiber alignment. 50-mm diameter split-cylinder specimens were prepared with steel fibers, steel wool fibers, and a combination of both. Specimens were loaded at two rates, from quasi-static to high rate servo-hydraulic. Each specimen was scanned using x-ray computed tomography (CT) both before and after loading such that internal damage could be measured. Crack measurements were made through a 3D analysis of load-induced crack area using a hybrid edge-detection/connected components analysis (macrocrack analysis). 3D digital volume correlation was applied to measure strains such that damage below the crack detection threshold could be inferred (microcrack analysis). Preliminary results showed that specimens loaded at a higher rate tended to show a higher degree of microcracking relative to macrocracking. However, this variation was of a similar order of magnitude to the variation obsrved due to differences in fiber alignment.

## 1 INTRODUCTION

High strength and ultra high strength concrete reinforced with various types of steel fibers has seen success in a wide range of structural and nonstructural applications for a generation. The combination of a high strength cement matrix with appropriately selected fibers can provide both strength and toughness, with the toughness being developed through an array of mechanisms, including fiber bridging and pullout, and controlled matrix cracking. In an effort to develop computational models based on elements of concrete and fiber morphology [1], prior work focused applying x-ray CT imaging to isolate and measure different internal energy dissipation mechanisms during fracture under flexural loading [2] and more recently, split cylinder [3]. In these studies, energy dissipation was well distributed between mechanisms of fiber pullout and matrix cracking. The work also quantified the effects of fiber orientation relative to stress field, and a method was proposed to bound the orientation effects through the use of an optimum and pessimum orientation for the specimens [3].

While this prior work answered some questions, additional questions remained. First, the experiments were all conducted at a quasi-static loading rate. As much of the modeling work was aimed at predicting performance under blast and ballistic loads, it becomes necessary to examine how the distribution of energy dissipation mechanisms changes as the loading rate is increased. Second, the limited resolution of the CT imaging meant that only cracks larger than the instrument resolution could be measured. A proper accounting of matrix cracking requires an estimate of microcracking that

occurs below the detection threshold. In order to address these two issues, a new round of split cylinder experiments was conducted on different formulations of fiber-reinforced high performance concrete. To address the first issue, specimens were tested at different loading rates ranging from quasi-static to low velocity impact. The goal being to examine if and how the energy dissipation mechanisms shift as the loading rate changes. To address the second issue, digital volume correlation (DVC) was applied to measure 3D strain fields as a proxy for microcracking below the scan resolution.

## 2 MATERIALS AND METHODS

### 2.1 concrete Specimens

The material used for this study may be considered a high performance concrete with a 115-120 MPa compressive strength. All specimens had a mix proportion of 1: 0.31: 0.60: 1.72: 0.21, by weight cement: silica fume: slag: sand: water. Three different specimen types were cast in 50 mm by 100 mm cylinders: plain concrete, concrete reinforced with "macro" fibers (Bekaert OL 0.2-mm diameter/13-mm long brass-coated), concrete reinforced with "micro" fibers (steel wool with diameter varying from 10 and 200 $\mu$m and length varying from 0.3 to 4.8 mm), and concrete reinforced with a combination of micro and macro fibers. Details of fiber contents are provided in Table 1.

**Table 1**: Concrete and Fiber Types

| Designation | Fiber Type | $V_f$ (%) |
|---|---|---|
| OL | macro | 2.0 |
| SW | micro | 1.5 |
| SWOL | macro/micro | 2.0+1.5 |

Specimens preparation consisted of mixing the cement matrix in a planetary mixer for five minutes, after which the fibers were added and mixed for an additional three minutes. Cast specimens were demolded after 24 hours, whereupon they were steam-cured at 90° for 72 hours. After cooling, the specimens were stored in ambient conditions until testing, which took place anywhere between 60 and 120 days. Each 50 by 100 mm cylinder was cut in half to form a set of two matched 50 by 50 mm nominal specimens. Each matched specimen pair was reassembled into its initial configuration prior to tomographic scanning.

### 2.2 X-Ray Computed Tomography

Prior to any mechanical testing, specimens were scanned with a laboratory-based x-ray CT scanner at 220 keV with a current of 245 $\mu$A. Tomographic scans consisted of 3770 projection images each being 2423 $\times$ 3770 pixels. Scanning time was 75 minutes. Tomographic reconstruction led to a series of 1200 $\times$ 1200 cropped slices at about 40 $\mu$m per voxel. An example slice image is shown in Fig. 1.

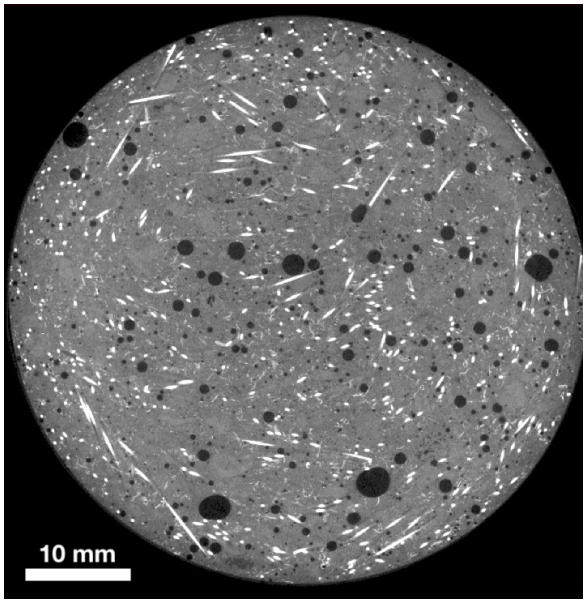


Figure 1: Tomographic slice of hybrid specimen. Macro fibers are solid white objects, while micro fibers are small white flecks in the concrete matrix.

From the resulting 3D tomographic images, a macro fiber orientation analysis was done for each specimen. The issue is that even a seemingly random fiber orientation is likely to have preferential alignments that can be significant [2]. In this analysis, the spatial orientation of each fiber is evaluated and compared to possible load axes in a split cylinder configuration.

An optimum orientation is defined as the position the fibers provide the most efficient reinforcement relative to the principal tensile stress. Conversely, a pessimum orientation is defined as that in which the fibers provide the least efficient reinforcement [3]. The intent of this analysis is to provide bounds on any subsequent analysis as to the role of fiber orientation in the result.

### 2.3 Mechanical Testing

After initial tomographic scan and fiber orientation assessment, each specimen was subjected to split cylinder loading. Two different loading rates were used:

- quasi-static ($\dot{\varepsilon} \approx 1 \times 10^{-3}$/s)
- intermediate ($\dot{\varepsilon} \approx 1 \times 10$/s)

Both cases were carried out on a servo-hydraulic load frame, while the third being performed on a drop weight tower. For the servo-hydraulic tests, position control was used. Load was recorded with a dynamic-calibrated load cell, and platen-to-platen displacement was recorded using a pair of LVDTs. For the drop tower tests, impact force was recorded with a dynamic load cell, and rebound height was measured with a digital camera.

Analysis of mechanical testing data is fairly straightforward, with the primary parameter of interest being energy dissipated by the specimen. For the servo-hydraulic-loaded specimens, this is simply established by taking the area under the load-deformation curve and subtracting the area of elastic recovery.

### 2.4 Image Analysis

internal damage is manifest by residual (inelastic) deformations in the material, which can be measured by comparing CT images before and after loading. Here, damage measurements were categorized as either macro cracks or micro cracks, with macro cracks being those visible in the CT images. Micro cracks are therefore those below the detection threshold of approximately 75 $\mu$m in width.

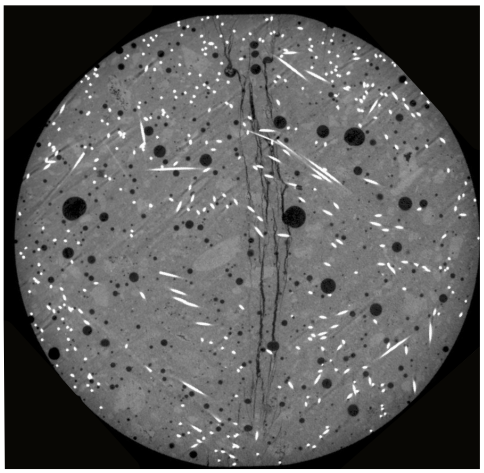

(a) Original slice

(b) Isolated macro cracks

Figure 2: Illustration of process to isolate internal cracks. Crack objects are isolated from pore objects through a registration with undamaged scan.

Isolation and measurement of macro cracks required several steps. As shown in Fig. 2a, internal voids and cracks are visible as dark objects in the specimen. All dark objects are then easily separated through an intensity-based image segmentation, however the resulting objects will include voids that are not of interest. Through a masking procedure in which images of undamaged specimens are aligned with damaged specimens, the air voids can be removed, leaving only the cracks as shown in Fig. 2b. Once the cracks are isolated, their properties such as surface area and crack width can readily be measured.

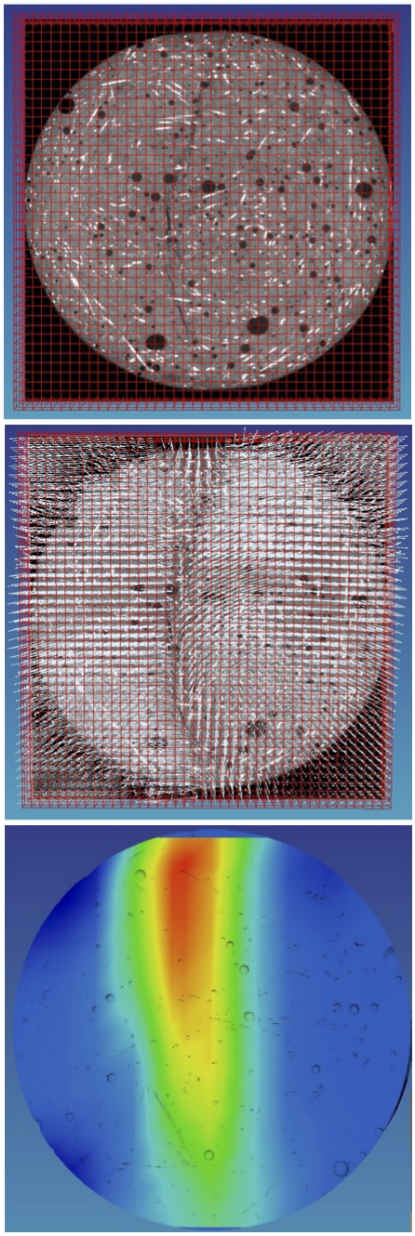

Figure 3: DVC illustration: top shows discretized domain, center shows displacement vectors for the domain, and bottom shows the corresponding lateral strain.

For micro crack measurement, since by definition they are not visible, we must rely on indirect ways to measure. In this work we employed a technique referred to as digital volume correlation (DVC), which is simply a 3D implementation of the more common digital image correlation (DIC) technique. Using CT images of an undeformed and a deformed specimen, DVC seek a displacement field such that the intensities at both positions in the deformed and undeformed are the same. As CT and other 3D imaging techniques have gained popularity, DVC has found a wide range of applications [4].

In DVC implementation the volume is divided into small subsets as shown in Fig. 3. The DVC code searches the reference (undeformed) image until it finds a voxel intensity pattern that matches that in the deformed image. The a displacement vector is then established as the difference in location between the two matched subsets. Strain fields can then be calculated from the displacement vectors. In this work, we make the assumption that any measured residual strains are the result of microcrack fields. That is, if the residual strains are measurable via DVC, they must be the manifestation of significant changes in the material, with microcracking being the most likely cause of that change.

## 3 EXPERIMENTAL RESULTS

### 3.1 Load-Deformation

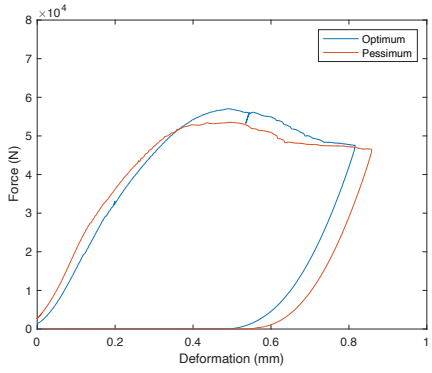


(a) Quasi-static loaded specimens

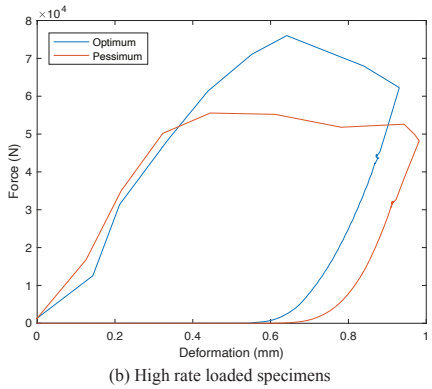


(b) High rate loaded specimens

Figure 4: Load-Deformation plots for specimens of different fiber orientation preferences.

Fig. 4 illustrates the characteristic load-deformation responses of the different specimens and loading rates. For both loading rates, the optimum fiber orientation leads to higher peak loads, although the effect was far greater for the high loading rate. As expected, the higher loading rate produced higher peak loads.

As previously noted, the mechanical energy dissipated by the specimen was taken as the area under the load-deformation curve, less the elastic unloading. Table 2 presents the net energy dissipated by the steel fiber-only (OL) specimens. Here, "High/Low" refers to the loading rate, while "Opt./Pess." refers to the specimen orientation. There are no conclusions to be drawn from the energy dissipation alone, since not all specimens were compressed to the exact same deformation. However, the numbers are necessary when evaluating the different modes of damage induced in each specimen.

**Table 2**: Specimen Energy Dissipation, $U$

| Specimen | $U$ $(J)$ |
|---|---|
| OL-High-Opt. | 39.8 |
| OL-High-Pess. | 37.6 |
| OL-Low-Opt. | 30.2 |
| OL-Low-Pess. | 31.3 |

## 3.2 Crack Analysis

As detailed above, 3D image analysis techniques were applied to the recorded CT images taken before and after the specimens were loaded. Macrocracks were defined as those visible in the CT images (crack width greater than roughly $75\mu m$), while microcracks were defined as those causing a residual strain, but were not otherwise visible in the images. For all specimens volumetric strain was measured using DVC. This measurement represents the total volumetric change in the specimen. However, we note that this volumetric change is made up of both microcrack and macrocrack components. As described in section 2.4, cracks were isolated and measured. An equivalent volumetric strain attributed to the macrocracks can be established by simply dividing the volume of the macrocracks by the volume of the specimen. Thus, the contribution of macrocracking can be separated from microcracking. Table 3 lists the measured volumetric changes in terms of macrocracking and microcracking. In order to account for the differences in actual energy dissipated by the different specimens, each of these strain values have been normalized by the energy dissipation presented in Table 2.

Table 3: Volumetric strain, $\epsilon_V$, and contributions from macrocracking, $\epsilon_{Mcr}$, and microcracking, $\epsilon_{\mu cr}$.

| Specimen | $\epsilon_V$ | $\epsilon_{Mcr}$ | $\epsilon_{\mu cr}$ |
|---|---|---|---|
| OL-High-Opt. | 0.00021 | 0.00011 | 0.00010 |
| OL-High-Pess. | 0.00027 | 0.00019 | 0.00007 |
| OL-Low-Opt. | 0.00021 | 0.00016 | 0.00005 |
| OL-Low-Pess. | 0.0.00025 | 0.00024 | 0.00001 |

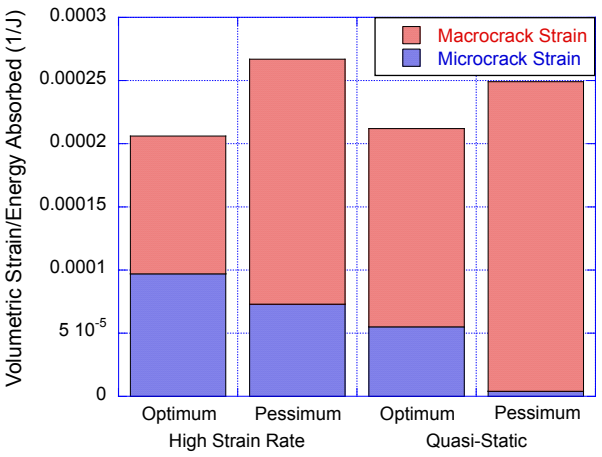


Figure 5: Relative distributions of microcracking versus macrocracking at different loading rates.

The relative strain values are better visualized through the chart of Fig. 5. Here, several distinct trends are highlighted. The first is that regardless of loading rate, optimally oriented specimens show lower overall volumetric change. What is more interesting, however, is that the increase in volumetric change in the pessimum-oriented specimens is entirely due to macrocrack opening. This is especially pronounced in the quasi-static specimen which

shows almost now residual strain due to microcracking. Nearly the entire volumetric change can be attributed to macrocrack opening.

An additional observation, though less pronounced, is that the specimens loaded at a higher rate show a higher degree of microcracking relative to macrocracking. This holds for both the optimum and the pessimum-oriented specimens.

## 4 Discussion

While the primary goal of this work was to quantify differences in energy dissipation mechanisms as a function of loading rate, we find that while there are measurable differences, these differences are within the bounds of differences that arise simply from differences in fiber orientation distribution.

The observed differences in microcracking versus macrocracking are best illustrated in the 3D renderings of Fig. 6. Here, we qualitatively observe how in the optimum-oriented specimen (Fig. 6a) the main tensile crack is not as wide, and tends to meander more compared to the pessimum-oriented specimen (Fig. 6b). This suggests that in the optimum-oriented specimens, the more advantageous fiber alignment makes it more difficult to open the macrocrack, forcing energy dissipation towards the formation of more microcracks. The exact same observation is made in comparing the observed changes when the loading rate is increased. At high loading rate, a higher degree of microcracking is observed regardless of the specimen orientation.

The observed differences in microcrack/macrocrack formation suggest differences in energy dissipation mechanisms. Crack formation, regardless of scale, represents an energy conversion in which strain energy is dissipated by formation of new surfaces. In the case of advancing macrocracks, there is a shift from surface formation (crack propagation) to crack opening. For fiber-reinforced composites, kinematically, crack opening means that fibers are being stretched and pulled out of the cement matrix, inducing a separate energy dissipation mechanism. Thus, we can conclude that both at low load rates and less-than-ideal fiber orientations, a much higher fraction of energy dissipation is provided by fiber pullout phenomena, such as debonding and friction. At high load rates and more ideal fiber orientations, however, we see a greater fraction of energy dissipation through matrix cracking.

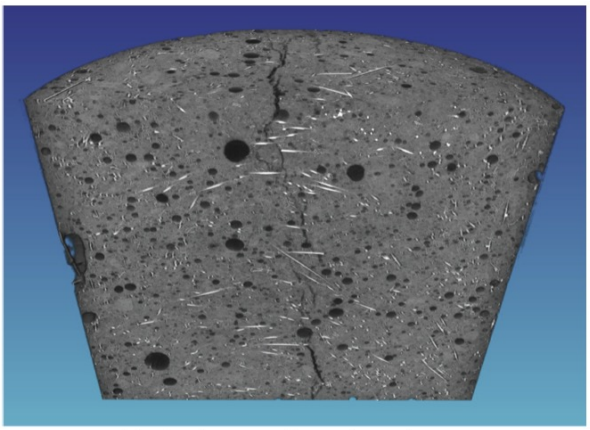

(a) Optimum-oriented specimen

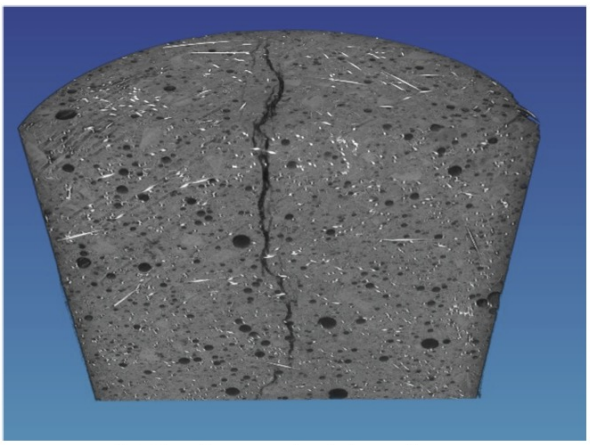

(b) Pessimum-oriented specimen

Figure 6: 3D renderings of internal cracking for: (a) optimum-oriented specimen and (b) pessimum-oriented specimen.

While the above observations are empirical, they do not necessarily address the root causes of the shift. From a load rate perspective, we can propose here that the shift in macrocrack-to-microcrack could have an inertial basis in that crack opening requires substantial rigid body motion, while microcracking does not. Hence, at higher rates the path of least resis-

tance is to create more microcracks, while at lower loading rates, when the inertial effects approach zero, the path of least resistance is to open up existing cracks.

With respect to the fiber orientation effect, it may be more simple. A poorly aligned set of fibers does not have the capacity to bridge macrocracks as well, so the crack can be opened more easily, negating the need to shift to additional microcracking. Indeed, in the results presented in Fig. 5, the fraction of microcracking is almost negligible, with macrocrack opening accounting for nearly all of the volumetric increase.

It must be noted that our microcrack/macrocrack definition is completely arbitrary, driven by the resolution of imaging capabilities. However, we suggest that it is likely that similar shifts would be observed at other scales, but we would likely see changes in the specific microcrack/macrocrack distributions.

## 5 CONCLUSIONS

In this work we employed x-ray CT imaging of undamaged and damaged fiber-reinforced high performance concrete specimens subject to split cylinder loading at different rates. The primary question to be answered was how the energy dissipation mechanisms during damage and fracture are affected by loading rate. Using a combination of 3D image processing techniques, two different damage types were designated: microcrack and macrocrack. 3D digital volume correlation was employed to measure the overall residual (inelastic) deformation of the specimens after testing. Concurrently, macrocracks, as defined as those cracks that were visible in the CT images, were isolated and measured, with a particular focus on the contribution of the macrocrack to the overall residual strain. A microcrack was then defined as anything that contributed to residual strain that was not measured as a macrocrack.

The results show distinct shift at higher loading rates, with a higher fraction of microcracking occurring at higher loading rates. This phenomenon was attributed to the inertial effects on macrocrack formation.

However, a distinct shift in microcrack/macrocrack distribution was also observed for matched specimens loaded at different orientations that maximize (optimum) or minimize (pessimum) the degree in which fibers are in a position to efficiently bridge cracking. At the optimum orientation, we see a higher contribution of microcracking compared to the pessimum orientation. This shift was attributed to the relative inefficiency of fiber bridging, easing macrocrack growth.

An important conclusion here is that while rate effects were seen in the damage patterns, the degree of variation between low and high rate loading was of a comparable magnitude as the degree of variation between optimum and pessimum specimen orientation. Thus, we cannot overemphasize the importance of taking fiber orientation into account in both modeling of such materials, or in the interpretation of experimental results.

In current work [5], additional experiments using a drop weight impact instrument ($\dot{\varepsilon} \approx 1 \times 10^2$/s) are being analyzed to further assess the shifts in energy dissipation mechanisms.

## REFERENCES

[1] Smith, J., Cusatis, G., Pelessone, D., Landis, E., O'Daniel, J. and Baylot, J. 2014. Discrete modeling of ultra-high-performance concrete with application to projectile penetration. *International Journal of Impact Engineering* **65**: 13–32. DOI: 10.1016/j.ijimpeng.2013.10.008.

[2] Trainor, K.J., Foust, B.W., and Landis, E.N. 2013. Measurement of energy dissipation mechanisms in fracture of fiber-reinforced ultrahigh-strength cement-based composites. *Journal of Engineering Mechanics* **139**(7): 771–779. DOI: 10.1061/(ASCE)EM.1943-7889.0000545.

[3] Landis, E.N., Kravchuk, R., Loshkov, D. 2019. Experimental investigations of internal energy dissipation during fracture

of fiber-reinforced ultra-high-performance concrete. *Frontiers of Structural and Civil Engineering* **13**: 190–200. DOI: 10.1007/s11709-018-0487-1.

[4] Buljac, A., Jailin, C., Mendoza, A. et al. 2018. Digital Volume Correlation: Review of Progress and Challenges. *Experimental Mechanics* **58**: 661–708. DOI: 10.1007/s11340-018-0390-7.

[5] Carlson, A.R. 2023. *Analysis of Loading Rate, Fiber Orientation and Material Composition Through Image Processing and Digital Volume Correlation in High Performance Concrete*. University of Maine, Orono Maine USA.